Chapter 4

Title: A New Technique to Calculate Kinetic and Thermodynamic Barriers for Estimation of Nucleation Rates and Interfacial Energy of $CaCO_3$ Prenucleation Nanoclusters at High Temperature using TGA Data

4. Introduction

The formation of stable nuclei, whether via supersaturation or the influence of high temperatures on solid-state processes, begins with nucleation.[259] During such nucleation, stable nuclei termed ultrasmall units of the solid phase are tuned up by aggregation, growth, crystallization, and phase transformation mechanisms, known as heterogeneous nucleation[260]. During this process, the involvement of interfacial surface is of significant importance and extensively explored in material interface synthesis[261], CO_2 sequestration[262], biomineralization[263], drug production[413], and industrial scaling control[414], and battery operations[264]. Exploring the nucleation pathways by adopting kinetic and thermodynamic networks out-turns the nucleation process, more understandable and clearer. Thus, the emphasis of the present study is on the role that kinetic and thermodynamic barriers play in influencing random nucleation during high-temperature solid-state processes. In order to perform the simulation associated with nucleation at high temperatures, an accurate estimate needs a firm grasp of kinetic and thermodynamic parameters. The effective nucleation rate is a product of $J_o = A_\alpha exp(E_a/RT)$ (Kinetic barrier) and $exp(\Delta G/RT)$ (Thermodynamic barrier), where, the nucleation activation energy, denoted by E_a, ΔG is free energy barrier of nucleation, and T is the temperature[415]. Surprisingly, while estimating the nucleation rate, accurate information on the computation of J_0 is hardly known, and most of the preceding studies have adopted J_0 as a constant term[265-267, 415]. A few experimental

research were carried out at room temperature for homogeneous nucleation to calculate $J_0\ as\ D/5d$, where D is the diffusion coefficient for monomers and d is the diameter of the monomer[416]. Additionally, more studies at room temperature were also used for computation of J_0 , by adopting an atomic force microscope (AFM). For example, J_0 for silica nucleation on NH_3/COO^- and carboxyl mixed hybrid substrates are as of $10^{14.8\pm1.4}$ and $10^{13.5\pm0.7}$ nuclei m^{-2} min^{-1}, respectively[269, 415]. Although such approaches are lacking for J_0 estimation in other nucleation systems, and no accurate estimation is elucidated for different systems reported so far at the higher temperature. These kinetic factors involved in nucleation and growth, i.e., nucleation's activation energy, are frequently ignored due to the complexity of microscopic operations and bulky calculation of reaction rate[417]. Consequently, in current research, we elaborate accurate computation of J_0 by estimation of both pre-exponential kinetic factor (A_α) and apparent activation energy of nucleation (E_a) precisely. These kinetic parameters A_α and E_a were experimentally computed by utilizing the utmost accurate iso-conversional methods by adopting non-isothermal thermogravimetric analysis (TGA) technology at higher temperatures. On the other hand, during the computation of activation energy through iso-conversional methods, by acquiring TGA data, multiple experiments runs at different heating rates are adopted, at specific conversion point. By doing multiple experimental runs, the accuracy in the reaction kinetics (i.e. activation energy) get enhanced when compared to single heating rate methods such as Coats–Redfern (CR[418]) and Distributed Activation Energy Model (DAEM[418]) models.[419] Moreover, isoconversional approach not assumes any particular reaction model like CR and DAEM models, led to generation of unique kinetic parameters at specific conversion[420]. Thereby, isoconversional methods are typically more accurate than single heating rate methods.

Inorganic material's in situ thermal decomposition trend in a controlled atmosphere can be easily obtained by mass loss vs time/temperature data extracted from non-isothermal TGA. Further, for the computation of the apparent activation energy, reaction conditions during the TGA scan can be easily altered by changing the measurement conditions like atmospheric gas, sample mass, heating rate, and heating conditions[421, 422].

Moreover, till now, the nucleation of crystalline calcite from amorphous calcium carbonate nanoparticles was investigated at 315 ^{0}C, and it's activation energy of dehydration was computed[423]. The nucleation rate of ultra-small osmium clusters to ultra-small crystals was computed by increment of temperature from 20 ^{0}C (1.02 nm) to 100 ^{0}C (1.31 nm), to be as 78.8 to 176.5 pm/min respectively[284]. In spite of above findings, there is no engineered technology to compute nucleation rate of ultra-small clusters at higher temperature (>100 ^{0}C). Thus, to make it possible, here we use the TGA technology for computation of nucleation rate ($nuclei\ \mu m^{-2}\ min^{-1}$) at higher temperature, as a first-time approach. On the contrary, in previous research, by using the TGA technology, the crystallization of In-Se in the high-temperature range (40 to 550 ^{0}C) was investigated by adopting DSC and TGA, and the activation energy of nucleation was computed through iso-conversional method[283]. Despite the analysis of nucleation of calcite crystal at a high temperature (315 ^{0}C) [283], nucleation rate (pm/min) computation of ultra-small osmium clusters (<1 nm) from 20 to 100 ^{0}C[284] and computation of apparent activation energy of nucleation for In-Se crystals in a high-temperature range (40 to 550 ^{0}C), the accurate computation of nucleation rate (J), interfacial energy, and thermodynamic parameters ($\Delta G, \Delta H\ and\ \Delta S$) for ultra-small clusters at high temperature (>100 ^{0}C), is still missing. Thus, there is an urgent need to calculate kinetic barrier (J_o) accurately with thermodynamic barrier for successful computation of nucleation rate at high temperature. For the accurate calculation of $J_o = A_\alpha exp(E_a/RT)$, we need to

calculate E_a and A_α accurately. The calculation of E_a and A_α comes under kinetic investigation of inorganic materials at high temperature. When determining the pre-exponential kinetic factor (A_α, min^{-1}) from TGA, it is necessary to incorporate the geometry of the nuclei in order to convert[415] A_α, min^{-1} to $A_\alpha, nuclei\ \mu m^{-2} min^{-1}$, during the event of nucleation. The geometry of the nuclei will significantly affect the nucleation rate, which is why the incorporation of the surface area of the nucleus is crucial[415]. Thus, after converting the unit of A_α from min^{-1} to $nuclei\ \mu m^{-2} min^{-1}$, J automatically gets converted to $nuclei\ \mu m^{-2} min^{-1}$ by utilizing eq. (22). Therefore, the choice of nucleation rate unit in terms of nuclei geometry is significant because it has a notable impact on the nucleation rate.

However, for the computation of the nucleation rate for ultra-small osmium clusters[284] between 20 and 100 °C, an aberration-corrected transmission electron microscope (TEM) is used, which is a subset of the TEMs and can achieve higher resolution when compared to a standard non-corrected TEM[424]. It is typically used for imaging and measuring atoms with high accuracy level in the order of 1 picometer. As a result, the nucleation rate for ultra-small osmium clusters can be calculated with high precision in picometers per minute (pm/min).[425]

These thermal degradation kinetic investigations of inorganic materials augment the formation of solid and gaseous products and have been emphasized over the centuries[426-429]. Moreover, among several inorganic nanomaterials investigated, calcium-based materials have gained compelling attention due to their incredibly high specific-surface area, non-toxicity, high interfacial energy, and faster chemical reactivity[288]. Specifically, $CaCO_3$ materials find their extensive application in versatile areas such as catalysis[430, 431], drug delivery[432-434], protein adsorption[435], cancer

therapy[436], energy storage carrier via 3rd generation solar power systems (CSP)[437], carbon nanotubes growth[438], and biomedical applications[439]. On the contrary, in regards to kinetics, apparent activation energy estimated for nano-sized calcium carbonate by different groups exhibited great variation ranging from 145 to 200 kJ/mol due to alteration of diffusion path in one dimension and two dimensions[293]. Despite the aforementioned investigations on thermal degradation kinetics on large $CaCO_3$ nanoparticles, no kinetic investigation was accorded for ultra-small $CaCO_3$ pre-nucleation clusters (CCPN) till now. Here, such $CaCO_3$ pre-nucleation clusters (1-2 nm) were used as a precursor for the computation of kinetic barrier J_0 at higher temperatures with the aid of TGA technology.

In today's scenario, comprehensive mathematical models that can render detailed analyses regarding reaction kinetics by computing morphological and energy barrier requirements to forecast the thermal stability of inorganic material are proposed [286]. Such energy barrier, i.e., the activation energy of the inorganic material, can be easily obtained by TGA for estimating the activation energy of nucleation by the kinetic data, and various model-free iso-conversional approaches, Friedman[440], Vyazovkin[441], and Vyazovkin-AIC[442], popularly employed by the different scientific communities for computation of activation energy.

Using the Friedman technique, systematic error is low when estimating activation energy, but this method becomes unstable due to slight experimental noise[440]. When using alternative isoconversional approaches to calculate activation energy, such as the Vyazovkin method, the averaging of the activation energy values from 0 to α can result in undesired flattening of the activation energy. This can lead to incorrect values of activation energy being generated at specific conversion.[420] To address this issue, Cai and Chen integral iso-conversional methods[291] was proposed in 2009, and is based on

equation (9). This method calculates activation energy over a small interval, Δα, due to which the reaction mechanism remains unchanged, due to very minute change in conversion values in the Δα (0.005) range. Consequently, this method presents extreme minute variations in activation energy values over the narrow interval Δα. Thus, mathematically, by integrating equation (9), with integral limits $T_{\alpha-\Delta\alpha}\ to\ T_{\alpha}$, over the small interval (Δα), the Cai and Chen method accurately determines the activation energy at particular point of conversion, as the reaction mechanism remains unchanged throughout the small interval Δα, and therefore the activation energy does not get averaged out over a range of conversions. This is main reason that iso-conversional methods, particularly the Cai and Chen integral iso-conversional methods, are considered to be more precise than conventional Vyazovkin methods, as well as approximation based linear integral iso-conversional methods like FWO and KAS.[291, 420, 443]

Given that the integrated iterative approach over a small conversion range (Δα) contained less relative error than the Vyazovkin AIC technique,[291] and required less computation time, we opted to use this method to accurately calculate the apparent activation energy of nucleation (E_a). As a result, the accuracy of the computed kinetic barrier of nucleation (J_o) was improved. During, computation of E_a, we took small value of $\Delta\alpha$ to be as 0.005, to improve the accuracy. On the other hand, for the computation of pre-exponential kinetic factor (A_a), temperature integral limits from $T_{\alpha-\Delta\alpha}\ to\ T_{\alpha}$ were also taken to be in small range (Δα=0.005) to enhance the accuracy. Thus, to the best of our knowledge, this is the first report for the accurate computation of J_o and A_α, for investigation of nucleation rate (J) of ultrasmall CCPN (Calcium carbonate pre-nucleation clusters) at high temperature, by using TGA technique. As the Kinetic barrier of nucleation (J_o) and nucleation rate (J) for ultra-small CCPN was computed for first time by using integral iterative method, thus we are saying it's a new approach for computation of J_o and J.

Current research uses computation of J_0 (kinetic energy barrier) at high temperature for inorganic material, BSA capped $CaCO_3$ prenucleation clusters (1-2 nm). A_α (pre-exponential kinetic factor) for CCPN was determined by adopting the differential function $f(\alpha)$ of the random nucleation process. To the best of our knowledge, this is the first time that TGA technology has been used to calculate the nucleation rates and interfacial energy of such ultra-small nanoclusters at high temperatures and respective conversions following the initiation of random nucleation within the CCPN matrix via breaking of the kinetic and thermodynamic boundary. The randomness of third-order nucleation was estimated by viewing distinct thermal mechanism routes using z(α) master plots. In addition, thermodynamic parameters (ΔG, ΔH, and ΔS) were conducted in order to illustrate the thermodynamic barriers necessary to induce random nucleation inside the CCPN matrix. Experimental validation for the nucleation of $CaCO_3$ pre-nucleation clusters to Calcite/CaS crystal was performed at the high temperature (500 ^{0}C).

4.1 COMPUTATIONS

Thermogravimetric analysis (TGA)

TGA (Perkin Elmer STA 6000/TGA 4000) was further performed to reveal the kinetics of CCPN at three heating rates 10, 15 and 20 ^{0}C/min. The CCPN powder was then heated from room temperature to 692 ^{0}C, under the N_2 gas flow rate of 20 ml/min. The N_2 gas was basically used to avoid the oxidation of the sample. Further, basically understand the mechanism of thermal degradation of CCPN, $z(\alpha)$ master plots were plotted. Furthermore, to compute activation energy with less systematic error, the iterative method is adopted, as presented below:

4.2 Computation of apparent activation energy of CCPN for random nucleation

The following equation delivers thermally activated kinetics for solid-state reactions:

$$\beta \frac{d\alpha}{dT} = \frac{d\alpha}{dt} = A_\alpha f(\alpha) \exp\left(\frac{-E}{RT}\right) \quad (1)$$

$$\alpha = \frac{m_0 - m_t}{m_0 - m_f} \quad (2)$$

Where, α is conversion, m_0 is initial weight of the sample, m_f is final weight of the sample remained after TGA, m_t is weight of the sample during increment of temperature via TGA. A_α is the pre-exponential kinetic factor in min^{-1}, t is the time in a minute, k is the reaction constant, T is the temperature in K, E is the apparent activation energy in kJ/mol, R is the gas constant (8.314 J/mol.K), $f(\alpha)$ model is the differential function, abbreviated as mechanism function, and β is the heating rate (^{0}C/min). The overall thermal degradation step constitutes of multiple reaction steps at a specific conversion point.[444]

Thus, as per the iso-conversational approach, kinetic investigation of inorganic materials was included under ICTAC kinetics committee recommendations[444]. Vyazovkin method[441] is used here to enhance the computational accuracy by considering temperature integral to estimate apparent activation energy (E_α), followed by estimation of activation energy at a particular point of conversion by minimizing the following

$$\varphi = \sum_{i}^{n} \sum_{j \neq i}^{n} \frac{J(E_\alpha, T_{\alpha,i})\beta_j}{J(E_\alpha, T_{\alpha,j})\beta_i} = minimum \quad (3)$$

In this equation,

$$J(E_\alpha, T_\alpha) = \int_0^{T_\alpha} exp\left(\frac{-E}{RT}\right) dT \quad (4)$$

But, while computing eq.(3), the value of activation energy gets averaged between 0 to α during the integration. Thus advanced iso-conversional technique proposed by vyazovkin[442] computes the apparent activation energy as a function of the extent of conversion. The main advantage of using such a technique is eliminating systematic error in the computation of apparent activation energy over a specific degree of modification. The advanced isoconversional process computes the apparent energy value by accepting the data collected on n^{th} temperature points.

$$\emptyset(E_\alpha) = \sum_{i}^{n} \sum_{j \neq i}^{n} \frac{J\left[E_{\alpha,} T_i(t_\alpha)\right]}{J\left[E_{\alpha,} T_j(t_\alpha)\right]} = minimum \tag{5}$$

Where,

$$J\left(E_{\alpha,} T_{i,j}(t_\alpha)\right) = \int_{T_{\alpha-\Delta\alpha}}^{T_\alpha} exp\left[\frac{E_\alpha}{RT_{i,j}(t)}\right] dt \tag{6}$$

The above integral was measured by performing numerical integration by the trapezoidal rule and its minimization is accomplished using the "Generalized Reduced Gradient algorithm" [445].

As vyazovkin AIC technique makes the minimization of function a time consuming process with no information regarding the derivative explicit expression. Thus, a more accurate approach was applied to computation activation energy using the iterative[446] linear method.

The following equation was used to develop the model in the iterative linear technique.

From eq.(1), we can get,

$$\beta \frac{d\alpha}{dT} = \frac{d\alpha}{dt} = A_\alpha f(\alpha) \exp\left(\frac{-E_\alpha}{RT}\right)$$

Upon integration of the above equation, the integral form of $f(\alpha)$ is evaluated as follows:

$$Z'(\alpha) = \frac{A}{\beta} J(E_\alpha, T) = \frac{AE_\alpha}{\beta R} Q(v) \tag{7}$$

$$= \frac{AE_\alpha}{\beta R} \frac{\exp(-v)}{v} \Psi(u) = \frac{ART^2}{\beta E_\alpha} h(v) \exp(-v) \tag{8}$$

Where, $J(E_\alpha, T)$ is approximated by the $\int_0^T \exp(-E_\alpha/RT)\, dT, and\ v$ is justified as E_α/RT, $Q(v)$ a more accurate temerature integral in comparison to $J(E_\alpha, T)$, which is defined by $\int_v^\infty \frac{\exp(-v)}{v^2}$.

The above-defined functions $\Psi(u)$ and $h(v)$ have numeric solutions instead of analytical solutions as for the functions $J(E_\alpha, T)\ and\ Q(v)$.

The iterative linear integral iso-conversional technique[446] is based on the following kinetic equation

$$Z'(\alpha, \alpha - \Delta\alpha) = \frac{A_{\alpha-\Delta\alpha/2}}{\beta} \int_{T_{\alpha-\Delta\alpha}}^{T_\alpha} e^{-E_{\alpha-\Delta\alpha/2/RT}} dT$$

$$= \frac{A_{\alpha-\Delta\alpha/2}}{\beta} \left[\int_0^{T_\alpha} e^{-E_{\alpha-\Delta\alpha/2/RT}} dT \right.$$

$$\left. - \int_0^{T_{\alpha-\Delta\alpha}} e^{-E_{\alpha-\Delta\alpha/2/RT}} dT \right] \tag{9}$$

These two integrals $\int_0^{T_\alpha} e^{-E_{\alpha-\Delta\alpha/2/RT}} dT\ and\ \int_0^{T_{\alpha-\Delta\alpha}} e^{-E_{\alpha-\Delta\alpha/2/RT}} dT$ has no analytical solution; thus, to solve the integral the following function was introduced as before,

$$J(E_\alpha, T) = \int_0^T e^{-E/RT}\, dT = \frac{RT^2}{E} e^{-\left(\frac{E}{RT}\right)} h(v) \qquad (10)$$

Where,

$$h(v) = v^2 e^v \int_v^\infty \frac{e^{-v}}{v^2} dv \qquad (11)$$

$h(v)$ has no analytical solution, so this integral is solved by Mathematica software (License Server 10.2.60.11, IIT BHU)

After using eq.(8), eq.(10) and eq.(11) and putting α and $\alpha - \Delta\alpha$ as limit for isoconversion, we get:

$$Z'(\alpha, \alpha - \Delta\alpha) = \frac{A_{\alpha-\Delta\alpha/2} RT_\alpha^2}{\beta E_{\alpha-\Delta\alpha/2}} \left[h(v) - \frac{v_\alpha^2 \exp(v_\alpha)}{v_{\alpha-\Delta\alpha}^2 \exp(v_{\alpha-\Delta\alpha})} h(v_{\alpha-\Delta\alpha}) \right] \exp(-v_\alpha) \qquad (12)$$

Where the subscript, $\alpha, \alpha - \Delta\alpha$ governs the conversion at specific points $\alpha, \alpha - \Delta\alpha$, respectively. On arranging eq. (12):

$$Z'(\alpha, \alpha - \Delta\alpha) = \frac{A_{\alpha-\Delta\alpha/2}}{\beta} \frac{RT_\alpha{}^2}{E_{\alpha-\Delta\alpha/2}} e^{-E_{\alpha-\Delta\alpha/2}/RT_\alpha} \left[h(v_\alpha) - \frac{v_\alpha^2 e^{v_\alpha}}{v_{\alpha-\Delta\alpha}^2 e^{v_{\alpha-\Delta\alpha}}} h(v_{\alpha-\Delta\alpha}) \right] \qquad (13)$$

Where, $v_\alpha = \frac{E_{\alpha-\Delta\alpha/2}}{RT_\alpha}$ and $v_{\alpha-\Delta\alpha} = \frac{E_{\alpha-\Delta\alpha/2}}{RT_{\alpha-\Delta\alpha}}$,

After rearranging eq.(13), we obtain

$$ln\left\{\frac{\beta_i}{T_{\alpha,i}^2\left[h(v_{\alpha,i})-\frac{v_{\alpha,i}^2 e^{v_{\alpha,i}}}{v_{\alpha-\Delta\alpha,i}^2 e^{v_{\alpha-\Delta\alpha,i}}}h(v_{\alpha-\Delta\alpha,i})\right]}\right\} = ln\left[\frac{A_{\alpha-\Delta\alpha/2}R}{E_{\alpha-\Delta\alpha/2}z'(\alpha,\alpha-\Delta\alpha)}\right]-\frac{E_{\alpha-\Delta\alpha/2}}{RT_{\alpha,i}} \quad (14)$$

$$ln\left\{\frac{\beta_i}{T_{\alpha,i}^2\left[h(v_{\alpha,i})-\frac{v_{\alpha,i}^2 e^{v_{\alpha,i}}}{v_{\alpha-\Delta\alpha,i}^2 e^{v_{\alpha-\Delta\alpha,i}}}h(v_{\alpha-\Delta\alpha,i})\right]}\right\} = ln\left[\frac{A_{\alpha-\Delta\alpha/2}R}{E_{\alpha-\Delta\alpha/2}z\left[\frac{A_{\alpha-\Delta\alpha/2}}{\beta}\int_{T_{\alpha-\Delta\alpha}}^{T_\alpha} e^{-E_{\alpha-\Delta\alpha/2}/RT}dT\right]}\right] - \frac{E_{\alpha-\frac{\Delta\alpha}{2}}}{RT_{\alpha,i}} \quad (15)$$

Where $i = 1,2,3 \ldots n,\ v_\alpha = \frac{E_{\alpha-\Delta\alpha/2}}{RT_\alpha},\ v_{\alpha-\Delta\alpha} = \frac{E_{\alpha-\Delta\alpha/2}}{RT_{\alpha-\Delta\alpha}}$ and $h(v) = v^2 e^v \int_v^\infty \frac{e^{-v}}{v^2}dv$

The first term of the right-hand side of eq.(14) is a constant for a specific degree of conversion.

For specific conversion, the plot of $ln\left\{\frac{\beta_i}{T_{\alpha,i}^2\left[h(v_{\alpha,i})-\frac{v_{\alpha,i}^2 e^{v_{\alpha,i}}}{v_{\alpha-\Delta\alpha,i}^2 e^{v_{\alpha-\Delta\alpha,i}}}h(v_{\alpha-\Delta\alpha,i})\right]}\right\}$ vs $\frac{1}{RT_{\alpha,i}}$ is a straight line having a slope of $E_{\alpha-\Delta\alpha/2}$. However, $ln\left\{\frac{\beta_i}{T_{\alpha,i}^2\left[h(v_{\alpha,i})-\frac{v_{\alpha,i}^2 e^{v_{\alpha,i}}}{v_{\alpha-\Delta\alpha,i}^2 e^{v_{\alpha-\Delta\alpha,i}}}h(v_{\alpha-\Delta\alpha,i})\right]}\right\}$ is a function of $E_{\alpha-\Delta\alpha/2}$. Thus, iterative procedure was adopted to compute the activation energy.

An iterative procedure to compute $E_{\alpha-\Delta\alpha/2}$ is performed until $\left|E^{n-1}_{\alpha-\frac{\Delta\alpha}{2}} - E^{n}_{\alpha-\frac{\Delta\alpha}{2}}\right| \leq \varepsilon$,

Where ε is the smallest possible positive quantity.

4.3 Computation of pre-exponential kinetic factor $(\mathbf{A_\alpha})$ of CCPN

The activation energy obtained by the above procedure is used to compute the value $A_\alpha f(\alpha)$.

Upon , integrating eq.(1) within the temperature integral limits from $T_{\alpha-\Delta\alpha}$ to T_α , will get

$$\frac{1}{\beta_i}\int_{T_{\alpha-\Delta\alpha,i}}^{T_{\alpha,i}} e^{-E_\alpha/RT}\,dT = \int_{\alpha-\Delta\alpha}^{\alpha}\frac{d\alpha}{Af(\alpha)} = \frac{\Delta\alpha}{[A_\alpha f(\alpha) - A_{\alpha-\Delta\alpha}f(\alpha-\Delta\alpha)]}$$

For above equation,

$$A_\alpha f(\alpha) - A_{\alpha-\Delta\alpha}f(\alpha-\Delta\alpha) = \Delta\alpha\beta_i\left[\int_{T_{\alpha-\Delta\alpha,i}}^{T_{\alpha,i}} e^{-E_\alpha/RT}\,dT\right]^{-1} \quad (16)$$

one can obtain,

$$A_\alpha f(\alpha) = \Delta\alpha\beta_i\left[\sum_{0}^{\alpha}\int_{T_{\alpha-\Delta\alpha,i}}^{T_{\alpha,i}} e^{-E_\alpha/RT}\,dT\right]^{-1} \quad (17)$$

According to the product of A_α and $f(\alpha)$ function, uppercase n governs the the leftside value of small range of conversion, we can get,

$$A_\alpha f(\alpha) = \Delta\alpha\beta_i \left[\sum_{J=0}^{\alpha-\Delta\alpha}\left[\int_{T_{n,i}}^{T_{n+\Delta\alpha}} e^{-E_{n+\Delta\alpha}/RT}\, dT\right]\right]^{-1} \quad (18)$$

Here, $f(\alpha)$ is the differentian function related to random nucleation process.

4.4 Calculating the CCPN's thermodynamic barriers, which are necessary for the start of random nucleation

As computation of kinetic parameters is necessary to uderstand the kinetic barrier for the random nucleation process, similarly computation of thermodynamic parameters are required to understand feasibility of the reaction, which governs initiation of the random nucleation process inside the CCPN matrix by breaking of the thermodynamic barrier.

The following equations[447, 448] are presented to calculate thermodynamic parameters ($\Delta H, \Delta G \; and \; \Delta S$),

Where, $\Delta H, \Delta G \; and \; \Delta S$ corresponds to change in enthalpy (ΔH), change in Gibbs free energy (ΔG), and change in entropy (ΔS), respectively.

$$\Delta H = E_\alpha - RT \quad (19)$$

$$\Delta G = E_\alpha + RT_p ln\left(\frac{K_B T_p}{hA}\right) \quad (20)$$

$$\Delta S = \frac{\Delta H - \Delta G}{T_p} \quad (21)$$

Here, K_B is boltzmann constant ($1.38064852 \times 10^{-23}\, J/K$), h is the plank constant ($6.62607004 \times 10^{-34}\, m^2 kg s^{-1}$), $T_p(K)$ is the peak temperature in DTG curve, $T(K)$ is the temperature at particular point of conversion.

Furthermore, the ΔH indicates the energy difference between the CCPN and the nuclei nucleated. Whereas, ΔS illustrates randomness and spontaniety of the system. It is important to note that small ΔS values means low reactivity of reacting species while ΔG repesents the presence of available energy to drive the nucleation.

4.5 Nucleation rate calculation using kinetic and thermodynamic barriers and interfacial energy calculation using thermodynamic barriers

A profound technique to estimate the nucleation rate is designated by the equation below:

$$J = J_0 exp\left(\frac{-\Delta G}{RT}\right) = A_\alpha exp\left(\frac{-E_\alpha}{RT}\right) exp\left(\frac{-\Delta G}{RT}\right) \quad (22)$$

In the above eq.(22), J is the nucleation rate in $nuclei\ \mu m^{-2}\ min^{-1}$, R is the universal gas constant $8.314 \frac{J}{mol.K}$, T is temperature in K. ΔG is the thermodynamic energy barrier of nucleation at high temperature[449] $\frac{J}{mol}$, which is directly related to interfacial energy (σ). $J_0\ in\ eq.(22)$ is related to kinetics of the system, that can be written as $A_\alpha\ exp\left(\frac{-E_\alpha}{RT}\right)$.[267, 415, 450]

After, taking the logarithm both the sides of eq.(22), we get the equation

$$\ln(J) = \ln A - \frac{(E_\alpha + \Delta G)}{RT} \quad (23)$$

And, The thermodynamic parameter[451] Z is defined by the equation below:

$$Z = \frac{16\pi v_o^2 \sigma^3}{3(k_B T)^3} \quad (24)$$

Where, v_0 is the molecular volume of the nanomaterial, σ is the interfacial energy of the nanomaterial. Molecular volume v_0 is defined as $\frac{M}{\rho_{nm} N_A}$, here M is the molar mass, ρ_{nm} is density of nanomaterial, and N_A is the Avogadro Number. Thermodynamic parameter, Z is defined by $\Delta G/RT$. To compute the interfacial energy against conversion and temperature, eq.(24) is used.

4.6 Experimental Section

4.6.1 Synthesis of CCPN

In brief, the current synthesis of BSA capped $CaCO_3$ pre-nucleation clusters was performed with slight modification[236]. In particular synthesis, 50 ml of 10 mM $CaCl_2$ (Avantor Performance Materials) was mixed with 15 ml of Moringa oleifera fresh leaves extract in a 250 ml conical flask, and then 1.77 gram of BSA protein (SRL Pvt. Ltd., India) was poured directly into the conical flask, followed by the addition of 5 ml DI water. Next, 2 ml of 1M aqueous ammonia (SRL Pvt. Ltd., India) was put into the conical flask dropwise, followed by the addition of 1 ml of 1 M NaOH solution (SRL Pvt. Ltd., India). Consequently, the whole mixture was allowed to react at 55 ^{0}C for 1 hour, and the same reaction mixture was incubated at 55 ^{0}C in the incubator for 15 hrs to complete the reaction.

4.7 Results and Discussion

The aqueous solution of CCPN was dried at 80 ^{0}C for 12 hrs to convert it to a solid-state nanoparticle. These dried nanoclusters were used for further characterization purposes like XPS, TGA, and FTIR. The drop-casting of CCPN was performed on the copper grid to examine the size with the aid of a TEM machine.

4.7.1 Physico-Chemical Characterization and Studies

TEM analysis (Tecnai G2 20 TWIN, FEI Company of USA (S.E.A.) PTE, LTD) was used to ascertain the size of CCPN. The image analysis (Image J software) of 100 nanoclusters yielded a Gaussian curve (Figure 4.1a), indicating the formation of 0.85 nm (mean diameter) large nanoclusters with the corresponding standard deviation of (σ) of 0.22 nm (Figure 4.1b). TEM images of ultra-small $CaCO_3$ Prenucleation clusters at different magnifications are shown in Figure 4.2. After addition of BSA protein (27mg/ml) to a solution with final pH of 10.7 resulted in the formation of a homogeneous CCPN solution (Figure 4.1c). After comparing the size of CCPN with other scientific details[236, 452], it was concluded that (CCPN) Calcium Carbonate Prenucleation clusters were capped by the BSA layer. Earlier studies have proved that the $CaCO_3$ prenucleation clusters are thermodynamically stable species and exist as ion clumps inside the aqueous solution[452]. In our previous research, the XRD analysis on the same $CaCO_3$ prenucleation clusters manifested its amorphous nature (Figure 4.3a)[236, 452]. But on close examination, the XRD analysis of $CaCO_3$ pre-nucleation clusters shows a low intensity peak of CaS only at one value of 2θ=31.4^0, as mentioned in Crystallography

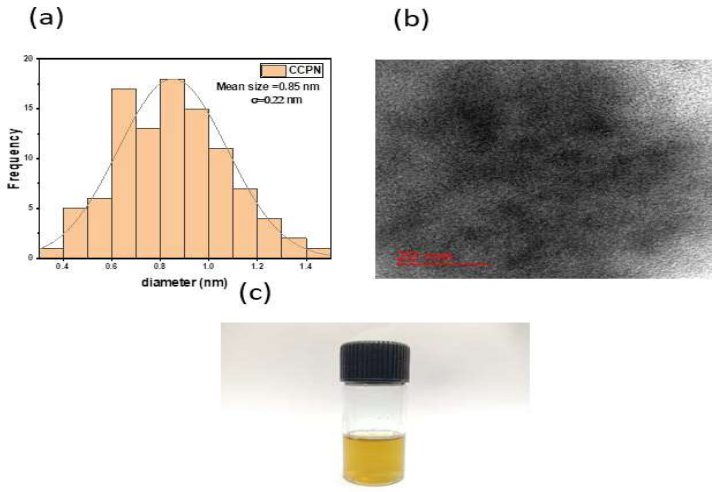

Figure 4.1 (a) Detailed histogram for CCPN clusters acquired by TEM (b) TEM image of CCPN clusters at 20 nm magnification (c) Ultrasmall CCPN clusters (0.5-1 nm).

Open Database (COD-9008606) (Figure 4.3a). The presence of low intensity single peak at 2θ=31.4^0 shows very little crystallinity of CaS formed via association of calcium with sulphur (S-H of BSA), at synthesis temperature (55 ^{0}C). However, at synthesis temperature (55 ^{0}C), no XRD peak is seen for calcite crystal formation (Figure 4.3a). On the contrary, for the experimental validation of the existence of nucleation in $CaCO_3$ prenucleation clusters at high temperature (500 ℃), these clusters were put in electrical furnance and heated to 500 ℃ at heating rate of 10 ℃/min under nitrogen atmosphere. After completion of nucleation inside the furnance, XRD analysis was carried out. XRD analysis of nucleated $CaCO_3$ prenucleation clusters shows intense peak of calcite at 2θ=29^0, which is matching with the high intensity peak of calcite crystal at 2θ=29^0, as mentioned in Crystallography Open Database (COD-9000970). (Figure 4.3b)

On the contrary, calcium and thiolate (S-H) of BSA are also nucleating together at 500 ℃ to form CaS crystals, which is authenticated by the experimental 2θ values of XRD at 31.4^0, 45.0^0, 56.1^0, 65.8^0, and 74.8^0, that closey matches with the 2θ values by COD database of CaS crystals (31.4^0, 45.0^0, 55.9^0, 65.5^0, and 74.5^0), (COD-9008606). (Figure 4.3b)

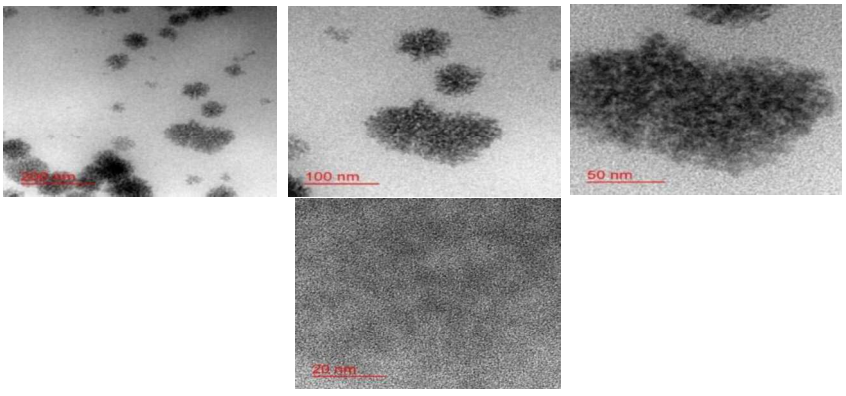

Figure 4.2 TEM images of $CaCO_3$ Prenucleation clusters at different magnifications.

So, these $CaCO_3$ prenucleation clusters after nucleation at 500 ^{0}C exist as a mixture of Calcite/CaS crystals. On the other hand, Calcium Carbonate Prenucleation clusters are too small to comprehend the presence of chemical bonds at the surface, so XPS analysis (Thermo Fisher Scientific) was performed to obtain detailed information on chemical bonds. XPS analysis (Figure 4.5a) indicated Ca2p1/2 peak deconvoluted into three components with binding energy 345.9 eV and 346.7 eV, 347.3 eV corresponds to the (Ca-S)[236], $CaCO_3$ formation [453, 454] capped with BSA, respectively. The Ca2p3/2 were deconvulated into three components with binding energy of 350.3, and 351.8 eV, corresponds to $CaCO_3$ and $CaCl_2$.[455] Furthermore, XPS investigation, exhibited formation of CCPN by acquiring leaf extract as reducing agent and BSA as a capping

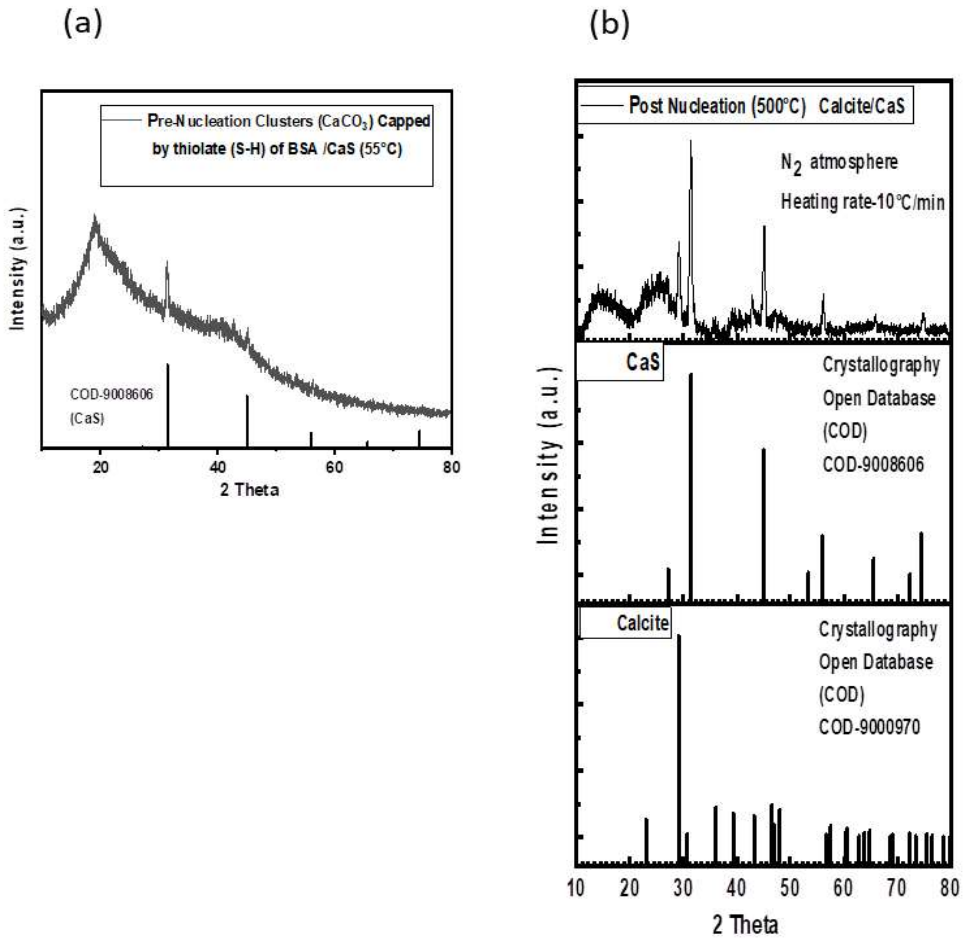

Figure 4.3 (a) XRD of $CaCO_3$ prenucleation clusters (b) XRD of Calcite/Cas formed after nucleation of $CaCO_3$ prenucleation clusters.

agent (Figure 4.5a). The leaf extract contains ascorbic acid in ample amount, and the mechanism of Carbonate ion formation is presented in Figure 4.4a[236]. When ascorbic acid (vitamin C) is present in an aqueous solution, electrostatic interactions between positively charged calcium ions and ascorbate ions result in the formation of calcium ascorbate complex.[345] Ascorbic acid may assist in binding more calcium ions, leading to the formation of an increased number calcium ascorbate complexes. As a consequence, O^- of the carbonate ions (CO_3^{2-}) may readily connect to calcium-attached complexes, and the rate of reaction between calcium ions and carbonate ions is accelerated, resulting in a quicker synthesis of $CaCO_3$ nanoparticles.[345] Moreover, by utilizing ascorbic acid as crystal and growth modifiers, it is possible to improve the synthesis process of $CaCO_3$ nanoparticles to achieve the uniformity, and the preferred morphology, including desired size and shape requirements.[345, 456] Since ascorbic acid is an antioxidant, it inhibits the oxidation of metals during nanoparticle formation and protects the surface of nanoparticles from oxidation.[457, 458] Consequently, in the absence of ascorbic acid, the rate of reaction for the fabrication of $CaCO_3$ would slow, desired shape, size, uniformity, and crystallinity cannot be achieved, and metals will be readily oxidized, leading to the development of metal oxides (CaO) rather than $CaCO_3$.

Moreover, to demonstrate the presence of functional groups on the surface of CCPN, FTIR (Nicolet iS5, THERMO Electron Scientific Instruments LLC) (Figure 4.5b)

$$\boldsymbol{2NH_3\,(aq.) + CO_2(g) \rightarrow NH_4^+(aq.) + NH_2COO^-(aq.)}$$

$$\boldsymbol{NH_4^+(aq.) + 2H_2O + \ NH_2COO^-(aq.) \rightarrow NH_3H_2O + NH_4HCO_3\,(aq.)}$$

$$\boldsymbol{NH_4HCO_3\,(aq.) \leftrightarrow HCO_3^-(aq.) + NH_4^+(aq.)}$$

$$\boldsymbol{HCO_3^-(aq.)\ + NH_3\,(aq.) \leftrightarrow NH_4^+(aq.) + CO_3^{2-}\,(aq.)}$$

(a) Carbonate Formation

Figure 4.4 (a) Mechanism of Carbonate ion synthesis.

analysis was acquainted. Whereas, such formations were also corroborated by absorbance (Figure 4.5c) by peak at 297 cm^{-1} shifted from 282 cm^{-1} (native BSA) [213] due to $\pi - \pi^*$ stacking indicating CCPN formation[236]. Furthermore, after completion of basic characterizations, TGA data were used to calculate $d\alpha/dt$, to compute reaction pathways and kinetics as shown below:

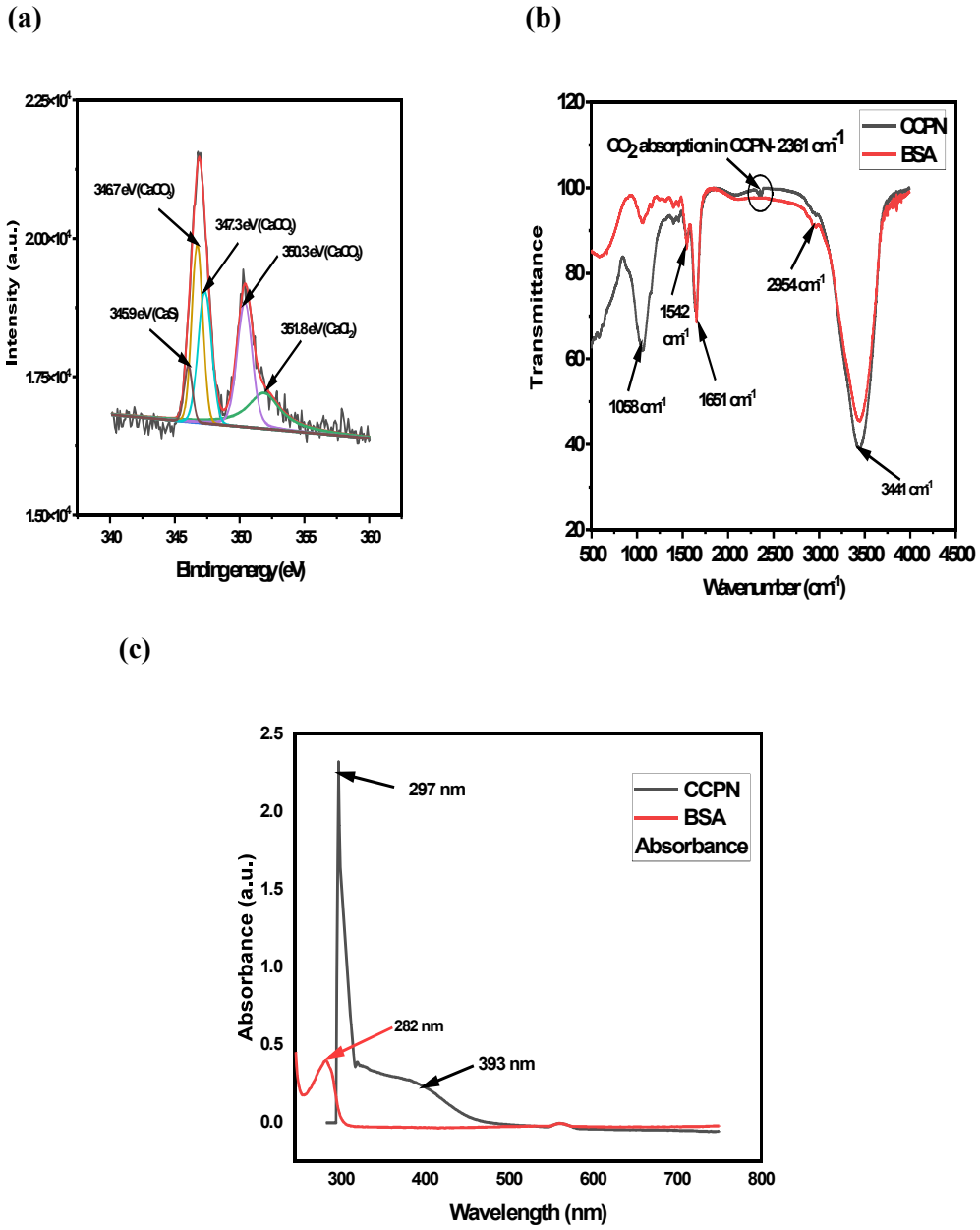

Figure 4.5 (a) XPS analysis for ultra-small CCPN clusters (b) FTIR analyses for CCPN and BSA protein from 500 to 4500 cm^{-1} (c) Absorbance of aqueous solution for CCPN and BSA protein together.

4.7.2 Reaction Kinetics and corresponding Pathways

Current study considered $CaCO_3$ prenucleation nanoclusters as precursor for further nucleation and growth at high temperature and further computation were performed.

Direct models, based on integral and differential approaches are elaborated in Table 1, providing essential understanding to systematic involvement of reactant phases. Besides, it also enhances the understanding of the thermal degradation pattern as a function of reaction progression (Figure 4.6a). To determine the reaction mechanism, the product of an integral and differential functions (Table 1), abbreviated as $z(\alpha)$ master plots[459], are plotted at three heating rates 10, 15, and 20 ^{0}C/min from conversion 0.1 to 0.85. Theoretical values of z(α) are calculated and plotted, and then compared to experimental values of z(α). If the experimental values coincide with the theoretical values at a specific conversion, or if they are close to any of the curves representing the theoretical z(α), then the reaction mechanism is determined based on the curve that the experimental z(α) coincides with or is closest to.

The above system of $z(\alpha)$ is abbreviated as $f(\alpha)\times g(\alpha)/f(0.5)\times g(0.5)$, by adopting $\alpha = 0.5$ as a reference[460]. The master plots pertaining to integral and differential models for the solid-state reaction are summarized in Table 1.

With reference to the half of the reaction progression for solid-state reaction, at high temperature,

The following equation can be written as,

$$z(\alpha) = \frac{f(\alpha)\times g(\alpha)}{f(0.5)\times g(0.5)} = \left(\frac{T_\alpha}{T_{0.5}}\right)^2 \times \frac{(d\alpha/dt)_\alpha}{(d\alpha/dt)_{0.5}} \qquad (25)$$

On the contrary, above $z(\alpha)$ master plot function $\frac{f(\alpha)\times g(\alpha)}{f(0.5)\times g(0.5)}$ were plotted with respect to α for individual governing, thermally active dynamic models, such as nucleation,

geometrical contraction, reaction order and diffusion models for solid-state decomposition. Since the derivative of reaction progression with time or temperature will be extracted out from experimental TGA data, we will utilize the experimental derivative approach to calculate the product ratios of the functions $\frac{f(\alpha)\times g(\alpha)}{f(0.5)\times g(0.5)}$. The plot will be drawn for different heating rates 10, 15, and 20 °C/min.

In Figure 4.6a, the term "0.5 conversion" refers to the point at which 50% of the $CaCO_3$ prenucleation clusters have undergone nucleation to form crystals. Additionally, these conversion points serves as a reference for computing the theoretical values of z(α) by eq.(25). By visualising the Figure 4.6a, upon variation in conversion in the range from 0.05 to 0.1, P4 reaction mechanism is observed. At 0.15 conversion, R1 (10 ^{0}C/min), A4 (15 ^{0}C/min), and R2 (20 ^{0}C/min) reaction mechanism are observed, which justifies the starting phase of nucleation. From, 0.2 to 0.85, $z(\alpha)$ experiment values closely matches with the $z(\alpha)$ theoritical values pertaining to R3 mechanism (Table 1). Where, R3 mechanism is linked to 3rd order random nucleation having three nuclei on individual particles, for degradation of CCPN matrix, by increment of temperature. In current resarch, reaction corresponds, the existance of nucleation between ions of $CaCO_3$ prenucleation clusters, at higher temperature and respective conversions. After computation of reaction mechanism/pathways activation energies for nucleation were computed by iterative method.

Table 1: Reaction Pathways for solid state reaction in terms of models governed by Integral function and Differential function.

Solid State Models	Integral function $g(\alpha)$	Differential function $f(\alpha)$
A1	$[-\ln(1-\alpha)]^{2/3}$	$\frac{1}{2}(1-\alpha)[-\ln(1-\alpha)]^{1/3}$
A2	$[-\ln(1-\alpha)]^{1/2}$	$2(1-\alpha)[-\ln(1-\alpha)]^{1/2}$
A3	$[-\ln(1-\alpha)]^{1/3}$	$3(1-\alpha)[-\ln(1-\alpha)]^{2/3}$
A4	$[-\ln(1-\alpha)]^{1/4}$	$4(1-\alpha)[-\ln(1-\alpha)]^{3/4}$
P2/3-Power law	$\alpha^{\frac{3}{2}}$	$\frac{2}{3}\alpha^{-\frac{1}{2}}$
P2- Power law	$\alpha^{\frac{1}{2}}$	$2\alpha^{\frac{1}{2}}$
P3- Power law	$\alpha^{\frac{1}{3}}$	$3\alpha^{\frac{2}{3}}$
P4- Power law	$\alpha^{\frac{1}{4}}$	$4\alpha^{\frac{3}{4}}$
F2- Contracting cylinder	$1-(1-\alpha)^{1/2}$	$2(1-\alpha)^{1/3}$
F3- Contracting sphere	$1-(1-\alpha)^{1/3}$	$(1-\alpha)^{2/3}$
D1- One-dimensional diffusion	α^2	$(1/2)\alpha$
D2- Two-dimensional diffusion (Valensi equation)	$(1-\alpha)ln(1-\alpha)+\alpha$	$[-\ln(1-\alpha)]^{-1}$
D3- Three-dimensional diffusion (Jander equation)	$[1-(1-\alpha)^{1/3}]^2$	$\frac{3}{2}[1-(1-\alpha)^{1/3}]^{-1}(1-\alpha)^{2/3}$
D4- Three-dimensional diffusion (Ginstling-Brounshtein equation)	$1-\frac{2}{3}\alpha-(1-\alpha)^{2/3}$	$\frac{3}{2}\left[(1-\alpha)^{\frac{1}{3}}-1\right]^{-1}$
R1- Random nucleation with one nucleus on the individual particle	$-\ln(1-\alpha)$	$(1-\alpha)$
R2- Random nucleation with two nuclei on the individual particle	$[(1-\alpha)^{-1}-1]$	$(1-\alpha)^2$
R3- Random nucleation with three nuclei on the individual particle	$\frac{1}{2}[(1-\alpha)^{-2}-1]$	$(1-\alpha)^3$

4.7.3 Analysis of apparent activation energy in opposition to reaction progression

As it is clearly visible from the Figure 4.6b, sinusoidal fluctuation of activation energy was observed for the CCNP degradation during the reaction progression, computed by iterative method.The iterative iso- conversional technique was adopted for computation of apparent activation energy from the slope of the straight line as mentioned in Figure 4.6c. By monitoring the variation of apparent activation energy with conversion as per specific sinusoidal pattern, eight important stages were identified to simulate the curve. In the course of first stage ($0.05<\alpha<0.2$), the apparent activation energy increases in linear

pattern from 53.147 kJ/mol to 161.042 kJ/mol. In the second ($0.2<\alpha<0.25$), third ($0.25<\alpha<0.35$), fourth ($0.35<\alpha<0.4$), fifth ($0.4<\alpha<0.45$), sixth ($0.45<\alpha<0.5$) and seventh ($0.5<\alpha<0.6$) and finally eighth ($0.6<\alpha<0.85$) stage, the reduction and increment in apparent activation energy values from 161.042 to 130.089 kJ/mol, from 130.089 to 156.319 kJ/mol, from 156.319 to 122.032 kJ/mol, from 122.032 to 149.194 kJ/mol, from 149.194 to 107.117kJ/mol, from 107.117 to 169.414kJ/mol, from 169.414 to 116.429 kJ/mol were observed sinusosidally, respectively. In sinusoidal wave, an increasing trend in activation energy values with the progression of reaction is mainly due to the formation of stable nuclei from ionic clusters during random nucleation with the evolution of heat, i.e., exothermicity[287]. On the contrary, decreasing the trend of activation energy with the progression of reaction is a sign of endothermic reaction. Moreover, such sinusoidal patterns in apparent activation energy values were also obtained while forming nucleated sodium carbonate (Na_2CO_3) crystals by utilizing data from a non-isothermal system with the aid of TGA.[461] We also compared apparent activation energy values extracted from different model-free isoconversional methods Vyazovkin, Vyazovkin AIC, and Iterative methods (Table 2). The most accurate Iterative and Vyazovkin and Vyazovkin AIC methods apparent activation energy values were found to overlap each other, at all conversion values (Figure 4.6b). While, Vyazovkin simulated values seems to be differ at most of the values of conversion.

Table 2: The values of apparent activation energy (E_α) computed by different iso-conversional methods.

α	Vyazovkin (kJ/mol)	Vyazovkin AIC (kJ/mol)	Iterative Method (kJ/mol)
0.05	44.244	60.848	53.147
0.1	65.878	76.766	74.370
0.15	96.813	107.656	106.336
0.2	156.35	161.716	161.042
0.25	153.825	127.724	130.089
0.30	133.064	127.826	128.2351
0.35	117.709	160.637	156.319
0.40	116.421	122.546	122.032
0.45	110.738	153.013	149.194
0.50	105.08	107.337	107.117
0.55	113.925	161.258	156.926
0.60	172.142	167.868	169.414
0.65	127.129	156.841	152.254
0.70	134.447	145.739	144.156
0.75	116.951	128.59	126.622
0.80	112.972	124.884	123.022
0.85	103.508	120.347	116.429

Derivative thermo-gravimetric (DTG) and TGA curves and DTG comparison for CCPN at three specific heating rates (10, 15 and 20 ^{0}C/min) are shown in Figure 4.7a-d. As the heating rate escalates from 10 ^{0}C/min to 15 ^{0}C/min and finally to 20 ^{0}C/min, the peak temperatures corresponding to maxima of mass-loss rates in the DTG peak shift towards right from 576.35K to 591.15K, and finally to 593.15K, respectively. The peak temperatures corresponding to two heating rates, 15 °C/min and 20 °C/min, are too close because of the deviation of sample and calibration temperature. This happened due to the creation of heat transfer limitations at higher heating rates, resulting in lower core temperature than the surface temperature of CCPN. Thus, an inert nitrogen gas requires a longer time to achieve equilibration between furnace and sample temperature at a higher

heating rate.[462]Moreover, at a close look at the heating rates of 10, 15, and 20 °C/min, the maximum rate of mass loss of CCPN occurs and it was found to be at 0.179, 0.444, and 0.447 mg/min, respectively (Figure 4.7d) for three heating rates. It is observed that increase in heating rates is well correlated with the maxima of mass loss rate. This increasing incremental heating rates can be well explained by heterogeneous nature of BSA capped CCPN, and its intricate structure[463]. Thus, mass and heat transfer resistance persist within the CCPN matrix at low heating rates. But, upon increment in heating rate, enhancement in mass and heat transfer driving forces were observed, leading to the termination of overall resistances inside CCPN matrix and accelerated mass loss rate.[464] On the other hand, reaction mechanism of CCPN decomposition is computed as random nucleation in the broad conversion range ($\alpha = 0.2\ to\ \alpha = 0.85$). Since nature nucleation is random, the pre-exponential kinetic factor will be calculated by adopting $f(\alpha)$ function from Table 1.

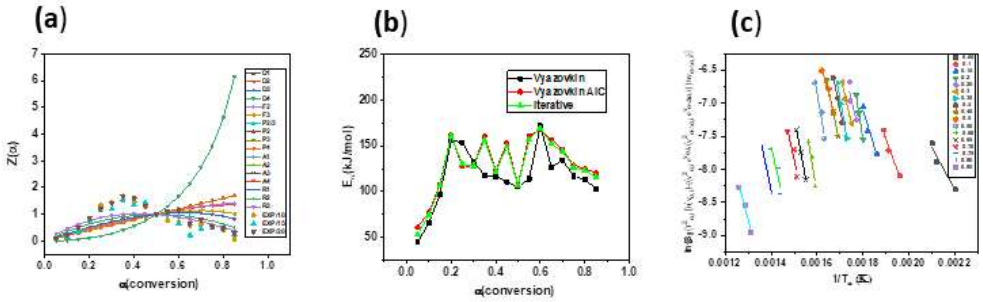

Figure 4.6 (a) Comparison of experimental and theoretical values (Product of integral and differential function) at different heating rates 10,15 and 20^0C/min by acquiring Z(α) master plots, CCPN (b) Variation of apparent activation energy (E_α)with conversion (α), as predicted by different iso-conversional techniques, CCPN (c) The plot of iterative iso-conversional method for computation of apparent activation energy (E_α) from the slope of Straight lines at respective conversions.

Table 3: Pre-exponential Kinetic factor A_α computed by differential function $f(\alpha)$ of Random Nucleation within CCPN matrix.

α	0.05	0.1	0.15	0.2	0.25	0.30	0.35	0.4	0.45
$A(min^{-1})$	$6.973x10^{4}$	$2.396x10^{6}$	$2.070x10^{9}$	$4.184 x10^{14}$	$4.092 x10^{11}$	$2.387x 10^{11}$	$7.666x 10^{13}$	$5.646x10^{10}$	$1.358x10^{13}$
$A\left(\frac{nuclei\ \mu m^{-2}}{min^{-1}}\right)$	$3.296x10^{20}$	$1.132x10^{22}$	$9.788x10^{24}$	$1.978 x10^{30}$	$1.934 x10^{27}$	$1.128x 10^{27}$	$3.624x 10^{29}$	$2.669x10^{26}$	$6.422x10^{28}$
α	0.5	0.55	0.60	0.65	0.70	0.75	0.80	0.85	-
$A(min^{-1})$	$2.663x10^{9}$	$4.223x10^{13}$	$1.511x10^{14}$	$3.964 x10^{12}$	$7.272 x10^{11}$	$1.267x 10^{10}$	$6.997x 10^{9}$	$7.376x10^{8}$	-
$A\left(\frac{nuclei\ \mu m^{-2}}{min^{-1}}\right)$	$1.258x10^{25}$	$1.996x10^{29}$	$7.146x10^{29}$	$1.874 x10^{28}$	$3.438 x10^{27}$	$5.991x 10^{25}$	$3.307x 10^{25}$	$3.486x10^{24}$	-

4.7.4 Computation of pre-exponential kinetic factor as a function of conversion

In the Figure 4.8a, variation of pre-exponential kinetic factor (A_α) vs reaction progression can easily be seen. The values of pre-exponential kinetic factor (Table 3) are calculated by utilizing eq.(17). Upon integrating the eq.(1) with lower and upper limit of temperature ($T_{\alpha-\Delta\alpha}\ to\ T_\alpha$) for a small interval $\Delta\alpha$, we can easily get eq.(18). The apparent activation energy values computed from iterative method were utilized for calculation of pre-exponential kinetic factors, which manifest the variation of kinetic factor in broad range (10^4 - $10^{14}\ min^{-1}$) (Table 3). This variation can mainly be due to complex and heterogeneous composition of CCPN matrix resulting from heterogenous thermal decomposition during various incremental temperature. The low value of pre-exponential factor ($A_\alpha < 10^9\ s^{-1}$), indicates slow surface nucleation, at specific conversion. On the contrary, high value of pre-exponential kinetic factor ($A_\alpha \geq 10^9\ s^{-1}$), leads to reactive bulk and surface nucleation simultaneously within the nanoclusters.[465] Moreover, for calculation of thermodynamic parameters, the previously calculated values of A_α and E_α has been used.

Table 4: Thermodynamic parameters required for CCPN nucleation at different heating rates and respective conversion.

	ΔH(kJ/mol)	ΔG(kJ/mol)	ΔS(kJ/mol)	ΔH(kJ/mol)	ΔG(kJ/mol)	ΔS(kJ/mol)	ΔH(kJ/mol)	ΔG(kJ/mol)	ΔS(kJ/mol)
α	10^0C/min			15^0C/min			20^0C/min		
0.05	49.420	144.020	-0.164	49.279	146.478	-0.164	49.237	146.811	-0.164
0.1	70.169	148.295	-0.135	70.053	150.318	-0.135	70.003	150.592	-0.135
0.15	101.87 7	147.860	-0.079	101.794	149.051	-0.079	101.744	149.212	-0.080
0.2	156.43 4	144.028	0.021	156.368	143.715	0.021	156.350	143.673	0.021
0.25	125.39 7	146.281	-0.036	125.332	146.822	-0.036	125.306	146.895	-0.036
0.3	123.49 4	147.011	-0.040	123.419	147.618	-0.040	123.385	147.700	-0.040
0.35	151.52 8	147.437	0.007	151.444	147.334	0.006	151.403	147.320	0.006
0.4	117.18 3	147.715	-0.052	117.108	148.499	-0.053	117.050	148.606	-0.053
0.45	144.28 7	148.604	-0.007	144.220	148.713	-0.007	144.145	148.728	-0.007
0.5	102.13 5	147.435	-0.078	102.077	148.595	-0.078	101.985	148.752	-0.078
0.55	151.84 4	150.900	0.001	151.795	150.870	0.001	151.702	150.866	0.001
0.6	164.19 1	157.278	0.011	164.157	157.091	0.011	164.090	157.066	0.011
0.65	146.89 8	157.566	-0.018	146.848	157.827	-0.018	146.756	157.862	-0.018
0.7	138.66 7	157.593	-0.032	138.617	158.063	-0.032	138.526	158.127	-0.033
0.75	120.88 3	159.465	-0.066	120.825	160.433	-0.067	120.709	160.564	-0.067
0.8	117.10 9	158.711	-0.072	117.042	159.752	-0.072	116.917	159.893	-0.072
0.85	110.10 8	162.899	-0.091	110.016	164.217	-0.091	109.867	164.395	-0.091

4.7.5 Computation of Thermodynamic parameters against the reaction progression

The values of thermodynamic parameters $\Delta H, \Delta G \; and, \Delta S$ are calculated by apparent activation energy, as shown in Figure 4.8b-d and Table 4. Furthermore, it was observed that $\Delta H \; vs \; \alpha$ plots at different heating rates coincided to each other, indicating its heating rate independent behavior. Similarly, other thermodynamic parameters like $\Delta G \; and \; \Delta S$ were also found independent of three heating rates (10, 15, and 20 ^{0}C/min), despite their dependency on peak temperature of different heating rates. It is observed that (Figure 4.8b) that during initial reaction progression, ΔH increases till α= 0.2 conversion and then

falls, giving sinusoidal pattern, which is repeated for the next conversion values. Such patterns indicate the increase and decrease in the endothermic nature of the reaction, indicates reaction progression, as explained previously by the plot of apparent activation energy vs conversion. Further, the difference between the averages values of E_α and ΔH is found to be 5 kJ/mol. This additional energy is required to break the reaction barrier for nucleation. On the other hand, a positive value of ΔG means, energy deficit in the nucleation and hence should be supplied to initiate the formation of activated complex/nuclei.[465] In the current research, ΔG values seems to be function of increasing conversion after $\alpha = 0.15$. In the conversion range, $0.15 < \alpha < 0.25$, $0.55 < \alpha < 0.6$, $0.7 < \alpha < 0.75$, and $0.8 < \alpha < 0.85$, a larger increase in ΔG was observed. Such increase in ΔG in four ranges of conversion, clearly indicates increment in the available

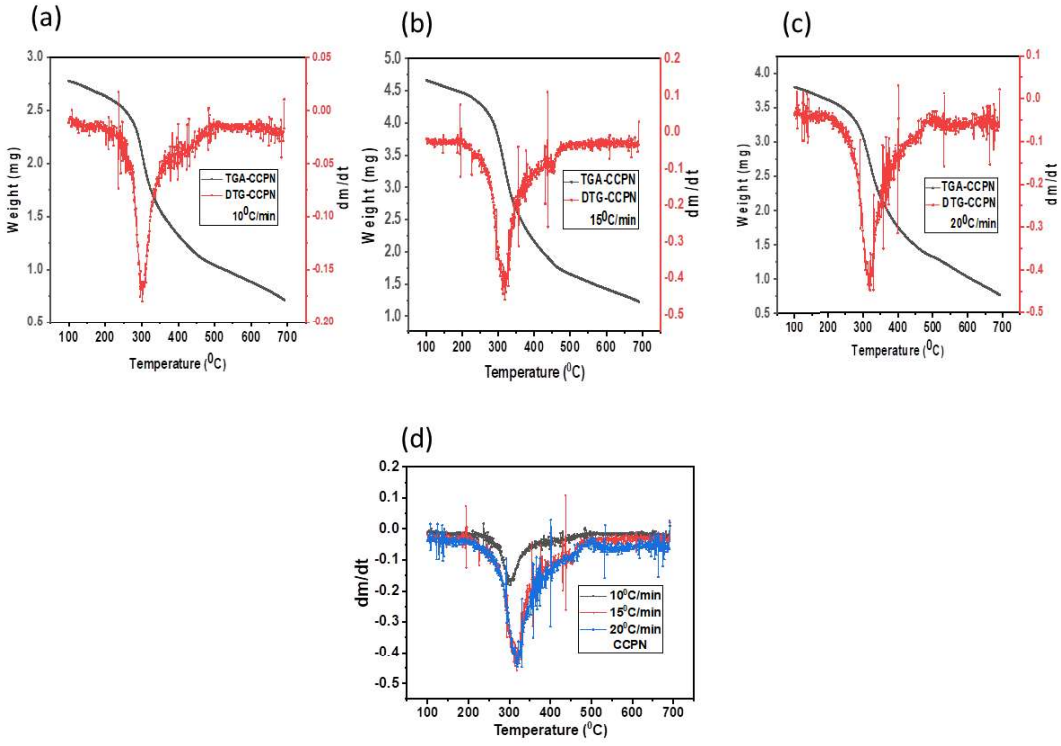

Figure 4.7 (a) TGA, DTG curve of CCPN at heating rate of 10°C/min (b) TGA, DTG curve of CCPN at heating rate of 15 °C/min (c) TGA and DTG curve of CCPN at heating rate of 20 °C/min (d) Comparison of DTG Curves of CCPN at different heating rates 10,15, and 20 °C/min.

energy for the nucleating clusters .[287] On the contrary, ΔS value hints towards randomness associated with the reacting system. A system with smaller ΔS, may indicates reconfigured physiochemical state of nanomaterial to achieve the thermodynamic equilibrium. In such case, the thermally decomposed nanomaterial may show little reactivity, consequently increasing its residence time leading to formation of activated complex/nuclei. While, a large value of ΔG, may indicate larger shift from the thermodynamic equilibrium. Consequently, the decomposing nanomaterial will show higher reactivity, and smaller residence time during the formation of activated complex. In our research, a close look on the graph of $\Delta S\ vs\ \alpha, \Delta S$ increases till 0.2 conversion and a sinusoidal wave in the plot is obtained as computed before, which shows subsequent increasing and decreasing pattern in the reactivity throughout the reaction. Similar pattern is followed by the $\Delta H\ vs\ \alpha\ plot$ (Figure 4.8b) indicating maxima and minima at specific conversion, also shown by $\Delta S\ vs\ \alpha$ graph (Figure 4.8d), justifying higher and lower reactivity at those conversion points. On the contrary, decrement in $\Delta S\ vs\ \alpha$ graph shows decrease in the system reactivity. Upon, coalescence of all thermodynamic results, it can infer that, throughout the reaction, reactivity goes up and down, but net effect is increase in the nucleation rate. Notice that during the course of measurements heat is being constantly and gradually added without interruption, to the nucleating system. This clearly indicates escalation in the free energy of nucleating system. Next, the thermodynamic parameters A_α and E_α are used to compute the nucleation rates.

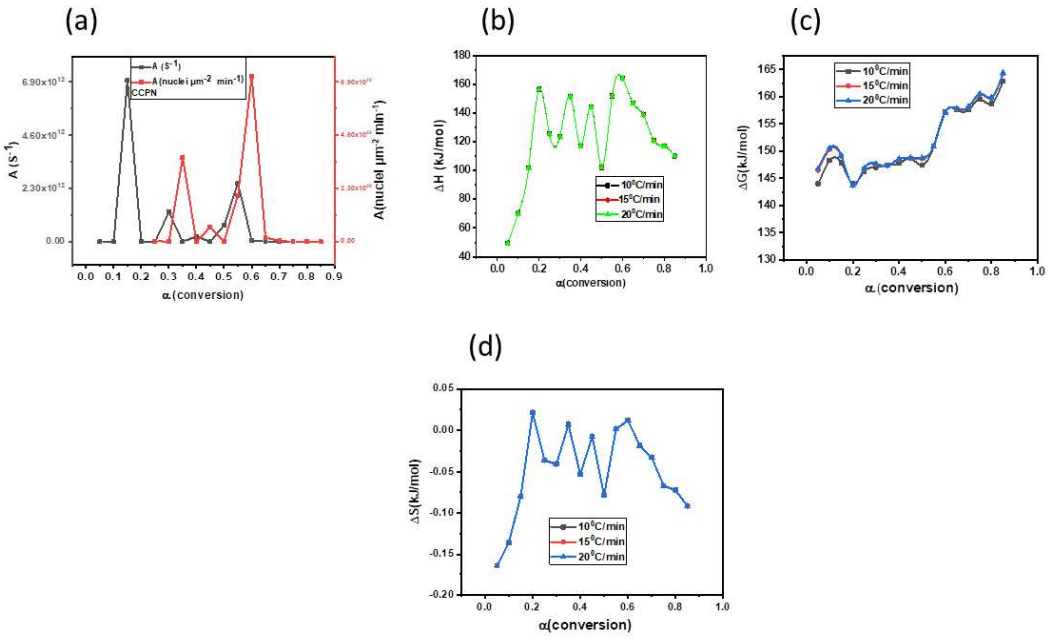

Figure 4.8 (a) The curve for pre-exponential kinetic factor (A_α) with reaction progression having units S^{-1} *and nuclei* $\mu m^{-2} min^{-1}$ at different heating rates 10, 15, and 20 ^{0}C/min, CCPN (b) The curve for Change in enthalpy (ΔH) with Conversion at different heating rates 10, 15, and 20 ^{0}C/min, CCPN (c) The curve for Change in Gibbs Free energy (ΔG) with Conversion at different heating rates 10, 15, and 20 ^{0}C/min, CCPN (d) The curve for Change in entropy (ΔS) with Conversion at different heating rates 10, 15, and 20 ^{0}C/min, CCPN.

4.7.6 Variation of nucleation rate with extent of conversion and Temperature

So far, a rigorous understanding of nucleation rates is lacking due to in-depth understanding of kinetic and thermodynamic parameters. In number of previous studies, kinetic term (J_0) in the eq. (22), was assumed to be a constant, rather than being computed. Besides, lacking high temperature nucleation rate analysis along with conversion were also not computed [265-267]. This cardinally happened due to minor importance of J_0 as compared to interfacial energy ascribed in the thermodynamic term[466]. However, at high temperature J_0 term becomes dominant factor in the analysis of nucleation rates[467]. Different studies have suggested a 10 fold variation in the nucleation rates due to assumption of constant J_o values at normal temperature

points[269, 468]. Consequently, computation of J_o was performed by determining A_α and E_α, using experimentally generated TGA data. A precise value of apparent activation energy (E_α) of nucleation for CCPN matrix is computed by iterative procedure (eq.(15)) and provided in Table 2. Whereas, the pre-exponential kinetic factor $A_\alpha, (min^{-1})$ is computed (Table 3) by performing the integration over small interval $\Delta\alpha$. Where, A_α is dependent on the $f(\alpha)$ differential function which is directly correlated to the random nucleation pattern (R3 mechanism), which is one of the important features of the current study. Notice that nucleation geometry is one of the essential feature [415] in pre-exponential kinetic factor (A_α) determation and nucleation rate. Consequently, $A_\alpha$value was converted in terms of nuclei geometry, leading to changed units as $nuclei\ \mu m^{-2}min^{-1}$. These computed values, substantially increased A_α and J values, (10^{20}→10^{30}) (Table 3) as nucleus volume and surface area were incorporated during the computation. Moreover, closer investigation of $J(nuclei\ \mu m^{-2}min^{-1})$ vs $T(K)$ (Figure 4.9a) plot, nucleation rate increases as the function of temperature. When temperatures is below 650 K, the nucleation rate remains relatively stable. However, once the temperature exceeds 650 K, the nucleation rate increases significantly and follows an exponential trend, as shown in Figure 4.9a.

In our investigation, an increasing trend in the values of nucleation rates is observed from 34.72 to 223416 $nuclei\ \mu m^{-2}min^{-1}$, from 95.137 to 342250 $nuclei\ \mu m^{-2}min^{-1}$, from 122.355 to 903260 $nuclei\ \mu m^{-2}min^{-1}$, at heating rates of 10, 15, and 20 ^{0}C/min, respectively (Table 5). Upon fitting the experimental data, a theoretical model is proposed to deduce the nucleation rate dependency on temperature. An exponential model $J = \omega_1 \exp\left(\frac{T}{\sigma_1}\right)$ was found to show best fit to the obtained data, plotted between the nucleation rate and reaction temperature (Figure 4.9a) (at all heating rates), where,

ω_1 and σ_1 are exponential function constants. The values of ω_1 and $\sigma_1$at different heating rates 10, 15, and 20 ^{0}C/min, are found as (2.244×10^{-5}, 33.013), (2.407×10^{-5}, 32.987), and (4.306×10^{-5}, 33.194), respectively. However, from the plot of nucleation rate vs conversion (Figure 4.9c) an exponential model $J = \omega_2 \exp\left(\frac{\alpha}{\sigma_2}\right) + J_0$, was also found as best fit, where, ω_2, σ_2 and J_0 are exponential function constants. The values of ω_2 , σ_2 and J_0 at different heating rates 10, 15, and 20 ^{0}C/min, are found as (1.298×10^{-4}, 0.039, -68.728), (6.774×10^{-5}, 0.038, 184.389), and (1.339×10^{-4}, 0.037, 401.163), respectively. From the eq.(23), the plot of lnJ vs $1/T$ gives a straight line, with the negative slope of $(\Delta G + E_\alpha)$ (Figure 4.9b). Many previous studies have shown the slope of lnJ vs $1/T$ gives$-(\Delta G + E_\alpha)$. [415]Moreover, Many preceding studies suggest that the nucleation rate increases exponentially as function of temperature[469], especially in the low (20 ^{0}C- 35 ^{0}C) and high temperature (580-680 ^{0}C) ranges [470-472]. Further, nucleation rates were also computed at different heating rates (10, 15, and 20 ^{0}C/min), it was observed that the nucleation rate increases, upon increment in heating rate (Figure 4.9a). This is due to the fact that heat and mass resistance are substantially decreased at higher temperature, leading higher nucleation rates. This phenomenon is clearly visible in the DTG curve of CCPN, as mentioned earlier. (Figure 4.7d) Next, thermodynamic barrier which initiates the random nucleation will be utilized, to compute the interfacial energy of CCPN.

4.7.7 Variation of Interfacial Energy with Temperature and Reaction Progression

Interfacial energy is typically defined as the excess internal energy per unit surface area arising from the formation of a new surface.[473] The internal energy of a material is the sum of the kinetic and potential energy of all its atoms and molecules.[474] As the temperature goes up, the atoms and molecules of the material will experience enhanced

kinetic energy, resulting in an increase in internal energy, or, in other words, a corresponding increase in surplus or excess internal energy of the material per unit area with increasing temperature, leading to an elevation in interfacial energy with temperature. Hence, the interfacial energy escalates as the temperature rises. In regards to the thermodynamic parameters, interfacial energies of many inorganic materials were addressed by several scientific communities in natural environments[475, 476]. But, in high temperature range (750-950 K), an investigation was put forward for computation of surface energy of copper nanoparticles by galvanic cell method[477]. This investigation computed values of surface energy of copper nanoparticles for the short temperature range (750-950 K). For instance, the interfacial energy for nucleation of $CaCO_3$ on silicates, at room temperature were calculated to be $30-50\ mJ/m^2$[265, 478]. In another investigations, the interfacial energy of $CaCO_3$ at room temperature via nucleation on quartz was computed to be $47\ mJ/m^2$ [478]. However, no studies were performed to assess the interfacial energy of $CaCO_3$ prenucleation clusters in BSA matrix, at higher temperature. In our investigation, an increasing trend in the values of interfacial energy with temperature is observed from 60.547 to 77.883 mJ/m^2, from 61.083 to 78.846 mJ/m^2, from 61.229 to 80.096 mJ/m^2, at heating rates of 10, 15, and 20 ^{0}C/min, respectively (Table 6). Our computed values of interfacial energy, found to be in good agreement with previous reported values of interfacial energy (30-50 $mJ/m^2$and 80-120 mJ/m^2) for $CaCO_3$ nanoparticles[265]. Upon close examination to the plot of Interfacial energy vs temperature (Figure 4.10a), it can be easily illustrated that, interfacial energy of CCPN varies as a function of temperature. The obtained interfacial data as function of temperature was found to fit a linear model $\sigma = p_1T + q_1$ (where $p_1$and q_1 linear function constants) at all heating rates. The values of $p_1$and q_1 at different

heating rates 10, 15, and 20 ^{0}C/min, are found as (0.0847, 13.836), (0.0852, 13.495), and (0.0841, 14.070), respectively.

Note that the effective interfacial energy is found to be independent of heating rate. It is important to note that data obtained for interfacial energy as a function of conversion (Figure 4.10b) very well fitted to a polynomial model of order 2, $\sigma = p_2\alpha^2 - q_2\alpha + r$, (where p_2, q_2 *and* r are polynomial constants) at all heating rates. The values of p_2, q_2, and r at different heating rates 10, 15, and 20 ^{0}C/min, are found as (35.793, 13.480, 62.536), (38.152, 15.913, 63.684), and (38.035, 14.305, 63.539), respectively. As finally we can note down that, as temperature increases, the nucleation rate increases exponentially, due to the increase in the value of interfacial energy i.e., surface energy with the temperature[479].

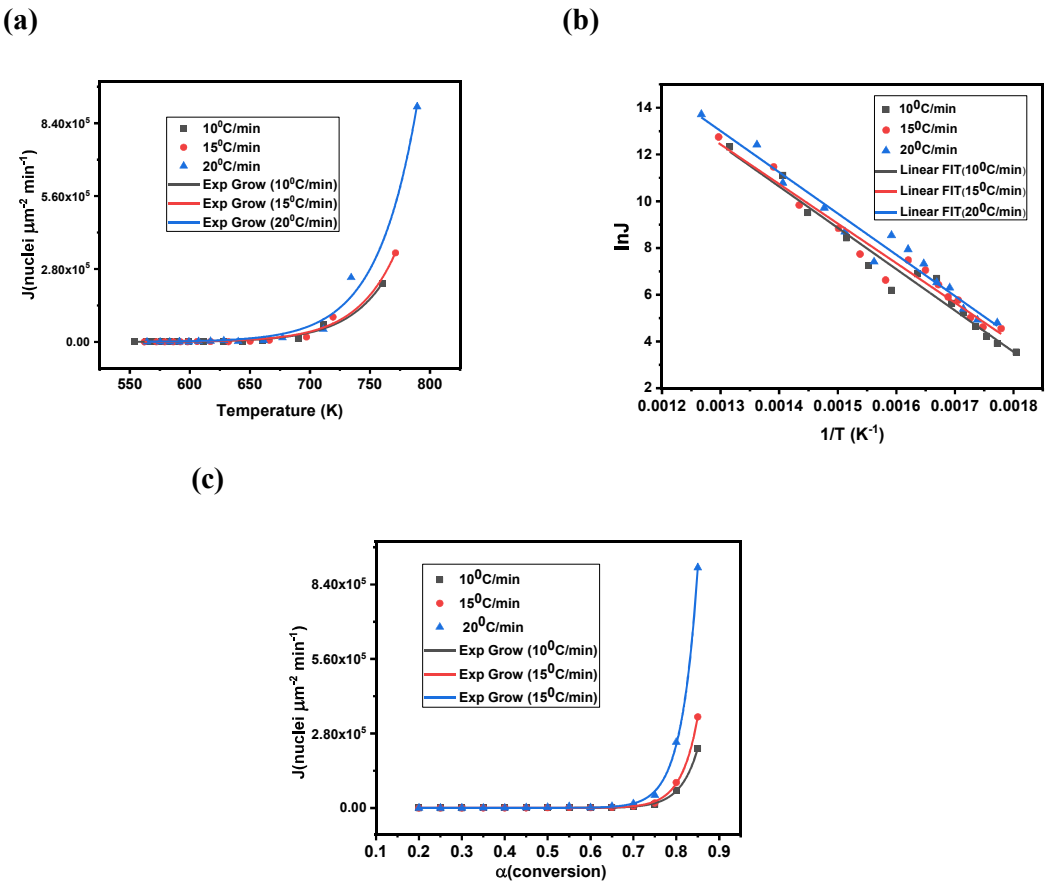

Figure 4.9 (a) Nucleation Rates curve for CCPN with temperature at heating rate of 10, 15 and 20 °C/min (b) Logarithm of Nucleation Rate Curve with reciprocal of temperature for CCPN at heating rate of 10, 15 and 20 °C/min (c) Nucleation Rates curve for CCPN with reaction progression at heating rate of 10, 15 and 20 °C/min.

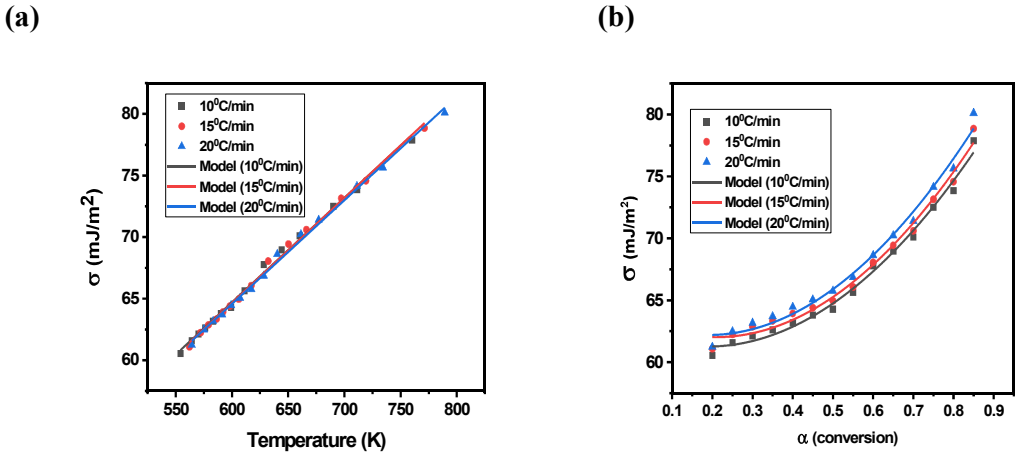

Figure 4.10 (a) Interfacial energy curve of CCPN with temperature at heating rate of 10, 15 and 20 ^{0}C/min (Linear Fit) (b) Interfacial Energy curve of CCPN with conversion at heating rate of 10, 15 and 20 ^{0}C/min (Polynomial FIT).

Table 5: Nucleation Rate computed by Kinetic and Thermodynamic barriers required for Random Nucleation within CCPN matrix with Temperature.

T(K)	$J(nuclei\ \mu m^{-2}\ min^{-1})$ 10 ^{0}C/min	T(K)	$J(nuclei\ \mu m^{-2}\ min^{-1})$ 15 ^{0}C/min	T(K)	$J(nuclei\ \mu m^{-}$ 20 ^{0}C/min
554.18	34.72455	562.17	95.13748	564.27	122.3559
564.23	50.13397	572.15	101.1517	575.27	136.5953
570.16	68.4128	579.23	149.723	583.24	218.2547
576.15	104.5096	586.28	319.317	591.29	542.8412
583.19	184.086	592.2	365.9787	599.21	681.3402
590.17	281.357	598.15	618.513	607.27	1516.247
599.2	810.6135	606.15	1156.889	617.26	2796.679
611.18	979.1765	617.15	1769.756	628.28	5125.673
628.19	487.8808	632.23	753.9746	640.25	1649.376
644.2	1413.347	650.18	2292.666	661.28	5966.318
660.17	4571.749	666.15	6879.988	677.17	16532.44
690.22	13372.15	697.2	18639.68	711.18	48260.13
711.17	66951.99	719.16	95511.43	734.28	247155.9
760.22	223416	771.25	342250.6	789.24	903260.8

Table 6: Interfacial energy computed by Thermodynamic barriers within the CCPN matrix with Temperature.

T(K)	σ(mJ/m^2)-10 ^{0}C/min	T(K)	σ(mJ/m^2)-15 ^{0}C/min	T(K)	σ(mJ/m^2)-20 ^{0}C/min
554.18	60.54739	562.17	61.08376	564.27	61.22982
564.23	61.59521	572.15	62.24673	575.27	62.48321
570.16	62.12895	579.23	62.87237	583.24	63.17393
576.15	62.62374	586.28	63.34082	591.29	63.69918
583.19	63.17253	592.2	63.93425	599.21	64.45315
590.17	63.803	598.15	64.39266	607.27	65.04773
599.2	64.2828	606.15	64.94835	617.26	65.76271
611.18	65.64312	617.15	66.0655	628.28	66.85688
628.19	67.78439	632.23	68.04771	640.25	68.61832
644.2	68.97325	650.18	69.43774	661.28	70.23108
660.17	70.11262	666.15	70.60539	677.17	71.39152
690.22	72.50914	697.2	73.14457	711.18	74.13929
711.17	73.8524	719.16	74.56685	734.28	75.63061
760.22	77.88349	771.25	78.84651	789.24	80.09687

Certainly, here's the condensed explanation with equations included:

The nucleation rate (J) according to Classical Nucleation theory (CNT) is determined using equations that account for both kinetic and thermodynamic barriers, which is written as follows:

$$J = \mathrm{Aexp}\left(\frac{-\mathrm{E}}{\mathrm{kT}}\right)\exp\left(\frac{-\Delta \mathrm{G}^*}{\mathrm{kT}}\right) \quad (1)$$

$$1\ mole\ of\ CaCO_3\ Clusters \ \rightarrow\ k = R \quad (2)$$

Putting the value of eq. (2) in eq. (1), we get

$$J = \mathrm{Aexp}\left(\frac{-\mathrm{E}}{\mathrm{RT}}\right)\exp\left(\frac{-\Delta \mathrm{G}^*}{\mathrm{RT}}\right) \quad (3)$$

According to Classical Nucleation Theory (CNT), the thermodynamic barrier ΔG^* can be expressed as below: (J. W. Mullin, Crystallization, Butterworth-Heinemann, Oxford, 1993[480])

$$\Delta G^* = \frac{16\pi\gamma^3 v^2}{3(kTlnS)^2} \quad (4)$$

After putting eq. (4) into eq. (3), we get, the value of J as

$$J = Aexp\left(\frac{-E}{kT}\right)exp\left(\frac{-16\pi\gamma^3 v^2}{3k^3T^3(lnS)^2}\right) \quad (5)$$

In eq. (5), the thermodynamic barrier to nucleation rate is expressed as

$$B^* = \frac{16\pi v^2\gamma^3}{3k^3T^3\,(lnS)^2} \qquad (6)$$

In our study, random nucleation was confirmed by analyzing z(α) master plots. In random nucleation, first nuclei form only when their size (r) matches the standard critical size of nucleation (r*), and this first nuclei formation takes place at particular temperature and the value of supersaturation (S) becomes 2.718. [481]. Here, we've found that the supersaturation value (S) is 2.718. By putting the value of S=2.718, the thermodynamic term B^* in eq. (6) becomes,

$$B^* = \frac{16\pi v^2\gamma^3}{3k^3T^3\,(ln2.718)^2}$$

$$B^* = \frac{16\pi v^2\gamma^3}{3k^3T^3\,(1)^2}$$

$$B^* = \frac{16\pi v^2\gamma^3}{3k^3T^3} \quad (7)$$

The above equation (7) is also employed as a thermodynamic parameter in estimating the nucleation kinetics of L-glutamic acid. [451] This thermodynamic term in eq. (7) is used to estimate interfacial energy variation with temperature.

$$\frac{\Delta G^*}{RT} = \frac{16\pi v^2\gamma^3}{3k^3T^3} \quad (8)$$

Eq. (8) can be written as

$$\gamma = \left(\frac{3k^3T^3\,\Delta G^*}{16RT\pi v^2}\right)^{1/3} \quad (9)$$

At 0.5 conversion and corresponding temperature of 600.17 K, eq. (9) can be computed as follows,

$$\gamma = \left(\frac{3 \times (1.38 \times 10^{-20})^3 \times (599.2)^3 \times 1.47 \times 10^8}{16 \times 8314 \times 599.2 \times 3.14 \times (6.13 \times 10^{-29})^2}\right)^{1/3}$$

$$= (265117.8)^{1/3}$$

$$= 64.24\ mJ/m^2$$

At 599.2 K, from eq. (5), according to Classical Nucleation Theory (CNT), we get

$$(B^*)_{CNT} = \frac{16\pi v^2\gamma^3}{3k^3T^3\,(lnS)^2}$$

$$\frac{\Delta G^*_{CNT}}{RT} = \frac{16\pi v^2\gamma^3}{3k^3T^3\,(lnS)^2}$$

$$\Delta G^*_{CNT} = \frac{16\pi v^2\gamma^3 RT}{3k^3T^3\,(lnS)^2}$$

At 599.2K, ΔG^*_{CNT} is expressed as,

$$\Delta G^*_{CNT} = \frac{16\pi v^2\gamma^3 RT}{3k^3T^3\,(lnS)^2}$$

$$= \frac{16 \times 3.14 \times (6.13 \times 10^{-29})^2 \times (64.24)^3 \times 8314 \times 599.2}{3 \times (1.38 \times 10^{-20})^3 \times (599.2)^3 \times (ln2.718)^2}$$

$$= 146992465.2\ mJ/mol$$

$$\boldsymbol{\Delta G^*_{CNT} = 146.9\ kJ/mol}$$

Therefore, at a conversion of 0.5 and a temperature of 599.2K, it is demonstrated that, ΔG^* calculated from Classical Nucleation Theory ($\boldsymbol{\Delta G^*_{CNT} = 146.9\ kJ/mol}$) and TGA

technique($\Delta G^*_{TGA} = 147.4\ kJ/mol$) comes out to be nearly same. Hence, at each conversion point ΔG^*_{CNT} **is same as that of** ΔG^*_{TGA} **.**

Given that at particular conversion and temperature, it is already demonstrated that, ΔG^* calculated from Classical Nucleation Theory and TGA technique comes out to be same, it follows that the variations in nucleation rate and interfacial energy with temperature and conversion will be consistent between the two theories, whether by TGA or CNT theory.

Conclusion

A powerful and appropriate technique was developed to accurately determine the apparent activation energy (E_α), Pre-exponential kinetic factor (A_α), Nucleation rates (J), Thermodynamic parameters $(\Delta G, \Delta H, \Delta S)$ and Interfacial energy (Υ) at higher temperature for ultrasmall $CaCO_3$ prenucleation clusters. An iterative procedure computed the average apparent activation energy (E_α) of 128.041 kJ/mol with little or negligible systematic error in the range $\Delta\alpha$. The differential function $f(\alpha)$ was found to vary as $(1-\alpha)^3$ upon monitoring the $z(\alpha)$ master plots, and this differential function was utilized to calculate A_α by performing integration from $T_{\alpha-\Delta\alpha}\ to\ T_\alpha$**.** The value of $A_\alpha(nuclei\ \mu m^{-2} min^{-1})$ was found to vary in the range $10^{20} - 10^{30}\ min^{-1}$, with respective conversions. According to proposed models, Nucleation rates were found to increase exponentially with temperature and conversion. The average value of Nucleation rate with temperature was found to be 22337 (10 ^{0}C/min), 33636 (15 ^{0}C/min), and 88140 min^{-1} (20 ^{0}C/min). While, Interfacial energy was found to vary linearly with temperature. A polynomial (Order 2) increase in the pattern of the interfacial energy is obtained with reaction progression. The average value of interfacial energy with temperature was estimated to be 66.77, 67.39, and 68.05 mJ/m^2 at 10, 15 and 20

^{0}C/min, respectively. Current study paves a way in nanoscience, use this method as accurate tool to examine the kinetics and thermodynamics dependent nucleation rates and surface energy in high temperature range. The reason of increase of interfacial energy with temperature was due to increase in surplus internal energy with temperature. As it is well known interfacial energy is called as excess internal energy. When the temperature of a system increases the corresponding interfacial energy also increases, and subsequence excess amount of internal energy also increses, which directly increases the interfacial energy values with temperature.